Clim Dyn (2017) 48:2471–2488
DOI 10.1007/s00382-016-3216-2

Boreal winter Arctic Oscillation as an indicator of summer SST anomalies over the western tropical Indian Ocean

Dao-Yi Gong[1] · Dong Guo[2] · Yongqi Gao[3,4] · Jing Yang[1] · Rui Mao[1] · Jingxuan Qu[1] · Miaoni Gao[1] · Sang Li[1] · Seong-Joong Kim[5]

Received: 2 December 2015 / Accepted: 1 June 2016 / Published online: 14 June 2016

Abstract The inter-annual relationship between the boreal winter Arctic Oscillation (AO) and summer sea surface temperature (SST) over the western tropical Indian Ocean (TIO) for the period from 1979 to 2015 is investigated. The results show that the January–February–March AO is significantly correlated with the June–July–August SST and SST tendency. When both El Niño/Southern Oscillation (ENSO) and the Indian Ocean Dipole (IOD) variance are excluded, the winter AO is significantly correlated with the regional mean SST of the western TIO (40°–60°E and 10° S–10°N), $r = 0.71$. The multi-month SST tendency, i.e., the SST difference of June–July–August minus April–May, is correlated with the winter AO at $r = 0.75$. Composite analysis indicates similar warming over the western TIO. Two statistical models are established to predict the subsequent summer's SST and SST tendency. The models use the winter AO, the winter ENSO and the autumn-winter IOD indexes as predictors and explain 65 and 62 % of the variance of the subsequent summer's SST and SST tendency, respectively. Investigation of the regional air–sea fluxes and oceanic dynamics reveals that the net surface heat flux cannot account for the warming, whereas the oceanic Rossby wave plays a predominant role. During positive AO winters, the enhanced Arabian High causes stronger northern winds in the northern Indian Ocean and leads to anomalous cross-equatorial air-flow. The Ekman pumping in association with the anomalous wind stress curl in the central TIO generates a significantly deeper thermocline and above-normal sea surface height at 60°–75°E and 5°–10°S. The winter AO-forced Rossby wave propagates westward and arrives at the western coast in summer, resulting in the significant SST increase. Forced by the observed winter AO-related wind stress anomalies over the Indian Ocean, the ocean model reasonably reproduces the Rossby wave as well as the resulting surface ocean warming over the western TIO in the subsequent summer. Observational analysis and numerical experiments suggest the importance of the oceanic dynamics in connecting the winter AO and summer SST anomalies.

Keywords Winter Arctic Oscillation · Summer SST · Tropical Indian Ocean · Prediction model

✉ Dao-Yi Gong
gdy@bnu.edu.cn

[1] State Key Laboratory of Earth Surface Processes and Resource Ecology, Beijing Normal University, Beijing 100875, China

[2] Climate Change Research Center, Chinese Academy of Sciences, Beijing 100029, China

[3] Nansen-Zhu International Research Center, IAP/CAS, Beijing 100029, China

[4] Nansen Environmental and Remote Sensing Center/Bjerknes Center for Climate Research, Bergen, Norway

[5] Division of Polar Climate Change, Korea Polar Research Institute, Incheon, South Korea

1 Introduction

Sea surface temperature (SST), particularly tropical SST, is one of the key factors contributing to multi-seasonal and inter-annual climate predictability. Improving climate prediction relies heavily on a better understanding of the mechanisms governing SST variability (NRC 2010). The Indian Ocean SST variability plays important roles in monsoonal climates. Previous studies found that El Niño/Southern Oscillation (ENSO) and the Indian Ocean Dipole (IOD) are two primary modes generating the inter-annual

variability of oceanic and atmospheric climates over the Indian Ocean and beyond with a certain persistence (Saji et al. 1999; Annamalai et al. 2005; Izumo et al. 2008; Schott et al. 2009; Xie et al. 2009; Taschetto et al. 2011; Taschetto and Ambrizzi 2012; Jiang et al. 2013; Zhu et al. 2015; Chakravorty et al. 2016; among others). With regard to the regional/local climate anomalies, the air–sea interaction and oceanic dynamic processes are two important mechanisms. In the tropical Indian Ocean (TIO; its longitude and latitude extent differs among authors and approximately covers 20°S–15°N and 40°–105°E), the air–sea interaction and the involved surface heat fluxes are reported to have significant influences on upper oceanic heat balance and mixed layer temperatures (Webster et al. 1999; Xie et al. 2002; Meehl et al. 2003; Wu et al. 2008; Xie et al. 2009; Rao et al. 2012). In these processes, the positive feedbacks among SST, surface wind and evaporation or the negative feedbacks among SST, cloud and shortwave radiation are important, depending on the climatological backgrounds (e.g., Li et al. 2002, 2003; Xie et al. 2002, 2009; Du and Xie 2008; Du et al. 2009; Wu and Yeh 2010; Xiang et al. 2011). Recently, Wu and Hu (2015) reported that the local surface heat fluxes over the Arabian Sea may make a small contribution before May but are important for local SSTs after May.

In addition, oceanic dynamics as the leading processes in sustaining and propagating the temperature variations (in particular the subsurface temperature) are well recognized. The oceanic Rossby wave is important in forming TIO variability at time scales ranging from intra-seasonal to inter-annual (Masumoto and Meyers 1998; Huang and Kinter III 2002; Xie et al. 2002; Jury and Huang 2004; Gnanaseelan and Vaid 2010; Webber et al. 2012; Trenary and Han 2012; Seiki et al. 2013; Chakravorty et al. 2014). Local or remotely connected wind stress anomalies dynamically cause regional Ekman pumping and further generate the forced Rossby wave. The presence of a downwelling Rossby wave is climatologically important. Along its westward propagation, the local upwelling is less active and the mixed layer and thermocline are deepened. These changes prevent the cold subsurface waters from being entrained into the surface layer. For example, during the strong 1997/98 El Niño event, the Rossby wave reached the western TIO in spring 1998, deepening the thermocline there by 60–80 m. Such a deepened thermocline is accompanied by warm SST anomalies, which further feed back into the western TIO atmospheric circulation and precipitation (Izumo et al. 2008; Du et al. 2009). Depending on the different atmospheric forcing patterns, the associated oceanic thermocline variations might be different. For example, those associated with the IOD are more closely confined to the region north of 10°S, while ENSO-induced thermocline variations are dominant south of 10 °S (Xie et al. 2002; Yu et al. 2005; Rao and Behera 2005; McPhaden and Nagura 2014; Sayantani and Gnanaseelan 2015). These Rossby waves are significantly intensified during El Niño and IOD co-occurrence years compared to those that occur during only El Niño or IOD years (Chakravorty et al. 2014). A theoretical baroclinic Rossby wave model simulation suggests that the large variability in the western southern Indian Ocean (approximately 8°–20°S) is primarily caused by a westward-propagating Rossby wave. This wave is driven by regional wind stress curl at 70°–95°E, while the oceanic influence from remote Pacific forcing is minor (Zhuang et al. 2013). In their oceanic general circulation model experiments, Tozuka et al. (2014) showed that without the westward downwelling Rossby waves, western TIO SSTs were significantly cooler than the control runs.

In addition to tropical forcing, mid- to high-latitude circulations, such as the Arctic Oscillation (AO)/North Atlantic Oscillation (NAO), are linked to TIO climates on timescales ranging from intra-seasonal to inter-annual. Observations suggest a two-way interaction at intra-seasonal timescales (e.g., Zhou and Miller 2005). The AO/NAO-associated atmospheric disturbances can cause TIO sub-seasonal anomalies (Pan and Li 2008; Lin et al. 2009; Yuan et al. 2011). In practice, the NAO can serve as a precursory signal for the Madden-Julian events with a leading time of approximately 10 days (Lin and Brunet 2011). Gong et al. (2014) showed that during positive AO/NAO winters, the enhanced Arabian High brings anomalous northern winds over the northern Indian Ocean. Meanwhile, the enhanced cross-equator air-flow results in simultaneously anomalous western winds, greater-than-normal precipitation, and a deeper thermocline in the central TIO.

In the present study, we report that after a positive winter AO, the SST in the subsequent summer over the western TIO experiences substantial warming. This phenomenon is caused by the arrival of the oceanic Rossby wave, which is generated in the central Indian Ocean by the anomalous AO-related wind stresses in winter. The remainder of the paper is organized as follows. Section 2 describes the data and methods used in the study. Section 3 first presents the statistical relationship between the winter AO and summer SSTs over the western Indian Ocean and then demonstrates the statistical models for predicting summer SST anomalies. In Sect. 4, the possible mechanisms connecting the winter AO and summer SSTs are investigated. The role of oceanic dynamics is tested by numerical experiments in Sect. 5. Finally, the major findings of the study are summarized, followed by a discussion in Sect. 6.

2 Data and methods

To examine the SST anomalies over the Indian Ocean, we employed monthly mean SSTs from the Extended Reconstructed Sea Surface Temperature dataset (ERSST v3b). The dataset has a resolution of 2° latitude ×2° longitude and was obtained from the National Oceanic and Atmospheric Administration (NOAA) (Smith et al. 2008). To analyze air–sea fluxes, we utilized the objectively analyzed air–sea heat fluxes (OAFlux; Yu et al. 2008) and examined the surface net heat flux (Q_{net}), the full-sky shortwave (SW), the full-sky longwave (LW), the turbulent latent heat flux (LH), and the turbulent sensible heat flux (SH). The monthly heat flux values used in this study spanned from 1979 to 2012 for turbulence fluxes and from 1985 to 2010 for the radiation and Q_{net}. All flux terms have a resolution of 1° latitude × 1° longitude. Because the OAFlux uses optimum interpolation sea surface temperature (OISST), we also analyzed OISST-v2 (Reynolds et al. 2002). The comparison between OISST and ERSST helped identify robust SST anomalies. The Simple Ocean Data Assimilation (SODA) product version 2.2.4 was used to investigate variations in sea surface height, the isotherm depth, and the subsurface temperature, which were updated as of December 2010. The spatial resolution of SODA was 0.5° longitude × 0.5° latitude, and of the total 40 vertical layers, the resolution for the uppermost levels was approximately 10 m (Carton and Giese 2008).

The AO and Niño3.4 SST were provided by NOAA's Climate Prediction Center. Here, the time series of the AO index was constructed by projecting 1000 hPa height anomalies poleward of 20°N onto the loading pattern of the AO mode and Niño3.4 SST was averaged SST anomalies over 5°N–5°S and 170°–120°W. The IOD's intensity was represented by an anomalous SST gradient between the western equatorial Indian Ocean (50°–70°E and 10°S–10°N) and the southeastern equatorial Indian Ocean (90°–110°E and 10°S–0°N) (Saji et al. 1999), computed using ERSST. In the present study, these climate indexes were confined to the period 1979 to 2015.

To focus on the inter-annual variability of Indian Ocean SSTs, all time series were high-pass filtered using a Butterworth filter. Only components with timescales shorter than 10 years remained and were employed in the subsequent analysis. Indian Ocean climate variations are tightly associated with ENSO and the IOD (e.g., Schott et al. 2009, among many others). Here, to highlight the possible AO signals, we removed ENSO and IOD variance from the variables of interest through multi-regression analysis. ENSO and the IOD have a phase-locking feature with mature peaks in boreal winter and autumn, respectively. We simply fit the preceding winter Niño3.4 SST and the autumn-winter IOD to all climate variables using the least-squares technique. Then, the estimated ENSO- and IOD-related components were subtracted from the original climate time series, and the residuals were regarded as ENSO-IOD-free parts and subjected to the subsequent analysis.

3 Winter AO index as an effective predictor of summer SST

3.1 Significant correlations

As discussed in the introduction, during the positive AO/NAO winter, the atmospheric Rossby wave was guided by westerlies. The wave tended to trigger persistent positive geopotential heights in the upper troposphere over approximately 20°–30°N and 55°–70°E on the inter-annual timescale. This effect was accompanied by a stronger Middle East jet stream and anomalous downward air motions. The enhanced Arabian High brought anomalous northern winds over the northern Indian Ocean. Consequently, a stronger cross-equator air-flow led to greater-than-normal precipitation in the central TIO as well as the anomalous in situ air–sea flux and upper ocean thermodynamics (Gong et al. 2014). Supposing that AO-related atmosphere-ocean anomalies in the TIO last for multiple months, our null hypothesis is that the winter AO may affect TIO SSTs in the subsequent seasons.

We investigated possible SST anomalies in association with the JFM AO by simply computing the ERSST regression upon the JFM AO index. To focus on the possible time lapses, we considered SSTs for every two-month segment from March through October. Instead of random noise, we found clear structures in anomalous SST fields. During March–April, the majority of SST anomalies were negative, which was likely due to JFM AO-related air–sea flux (Gong et al. 2014). In May–June, negative SSTs were replaced by positive anomalies in the tropical Indian Ocean west of 60°E. The significant warming became much stronger in July–August: >0.2°C in a large region west of approximately 55 °E (Fig. 1). The signals in the western TIO sharply weakened in September–October and disappeared afterward. For comparison, we computed the OISST changes corresponding to the JFM AO and plotted them together with the ERSST regressions. The two datasets yielded very similar features (Fig. 1). The positive anomalies first appeared in May-June in the western TIO and were much larger in July-August. The spatial patterns and anomaly magnitudes of the ERSST and OISST regressions matched each other quite well. For simplicity, in the following sections, we only show results from ERSST.

Note that the regression analysis was performed based on the residuals after high-pass filtering and removal of ENSO/IOD. The AO-SST linkage, if physically robust, should emerge in the raw observations. Furthermore, the

correlation/regression analysis ignored the possible nonlinearity of the links and might have missed the difference between the ENSO types and phases that had different climate consequences (e.g., Weng et al. 2007; Kug et al. 2009; Wang et al. 2013). For clarification, we examined the SST composites based on the JFM AO index. The possible effects of ENSO and the IOD should be excluded, which is usually accomplished by setting a threshold (for example, 0.5 times of the standard deviation) to identify ENSO and IOD years. Unfortunately, we found that when a strict threshold was applied, it was difficult to select enough samples for the AO composite. For example, if we applied a stricter criterion of $|\mathrm{IOD}| < 0.5\sigma$ (both in the preceding and in the simultaneous autumn) and $|\text{Niño3.4 SST}| < 0.5\sigma$, only three ENSO and IOD neutral years were recorded: 1979 (AO= −1.25), 2004 (AO= −0.97), and 2014 (+0.09). Of these 3 years, only one was a significant negative case with AO< −1 and none had a positive counterpart. It seemed that 0.9 times the standard deviation was an acceptable threshold. Therefore, we selected the positive AO cases when the AO was larger than one unit and when DJF Niño3.4 SST and the SON IOD were both within 0.9 times the standard deviation. Three identified positive AO cases included 1990, 1993 and 2002. Similarly, three negative AO years identified were 1979, 1980, and 2001. The difference between positive means minus negative means was computed, and the corresponding significance was estimated using a two-sample *t*-test. As shown in Fig. 2, slightly positive anomalies appeared in the TIO west of 55°E in May-June, but SST warming was not statistically significant. Interestingly, in the subsequent July-August, significant positive SST anomalies appeared in the western TIO. The >0.2°C anomalies covered a large region of approximately 7°S–7°N west of 65°E with a maximum of >0.4°C west of 55°E. The location and spatial extent of significant SSTs in summer were almost identical to those in the regression analysis (see Figs. 1c, 2c). When more data samples were used for compositing, the features remained unchanged and became even more robust (right panel in Fig. 2). An example was when we defined the AO > 0.3 and the AO < −0.3 as positive and negative events, respectively, and identified 4 positive cases (1982, 1990, 1993 and 2002) and 10 negative cases (1979, 1980, 1981, 1984, 1986, 1988, 1996, 2001, 2004 and 2005). To investigate the possible symmetry in the relationship in view of the positive and negative AOs, we computed mean SST anomalies for the 4 positive and 10 negative AO years, respectively. The positive anomalies of 0.2–0.3°C appeared over the western TIO during the positive AO cases. Meanwhile, cooling at a similar amplitude in the western TIO was found in the negative AO cases (figures not shown). SST changes corresponding to the AO phases appear to be nearly symmetrical. Generally, composites displayed features that were highly similar to those of the regression analysis, likely manifesting the winter AO-summer SST linkage again.

To reveal the details of SST anomalies through the seasons, we further investigated the monthly SST variations. We selected the region of 10°S–10°N and 40°–60°E, where the largest SST anomalies were located, to construct a regional mean SST time series. Then, the cross-correlations between the JFM AO index and the SST time series were computed for each month. The correlation increased substantially from spring to summer (Fig. 3). The three largest correlations appeared in July (0.70), August (0.60) and June (0.49); all were significant at the 0.01 level. After October, the correlations became insignificant. Note that both ENSO and the IOD affected Indian Ocean SSTs, persisting for multiple seasons. For clarification, we also computed the correlations between SST and the preceding December-January-February Niño3.4 SST as well as between the preceding September–October–November IOD. As shown in Fig. 3, a prominent feature was that the correlations for both Niño3.4 SST and the IOD decayed rapidly from spring to summer. For Niño3.4 SST, the correlation decreased from 0.79 in April to an insignificant value of 0.30 in August. For the IOD, the correlation decreased from 0.45 in April to 0.14 in August. These findings are consistent with those reported in previous studies (e.g., Du et al. 2009; Xie et al. 2009; McPhaden and Nagura 2014; Kumar et al. 2014; Sayantani and Gnanaseelan 2015). In a word, the JFM AO-related strong SST anomalies in the western TIO were obviously different from those in ENSO/IOD. For the former, the maximum warming occurred in summer, while for the latter, their signals decayed rapidly after the subsequent spring. As shown in Fig. 4, regional mean summer SST strongly co-varied in phase with the JFM AO index. Their correlation coefficient was 0.71. Note the feature of SST correlations increasing from spring to summer. We defined this multi-month SST tendency as an SST difference (△SST) of June–July–August minus April–May. The SST tendency was correlated with the JFM AO at $r = 0.75$ (Fig. 4).

3.2 Prediction models using the AO, ENSO and the IOD

The high correlation between the AO and SST implies that the JFM AO index has practical utility as a potential predictor of summer western TIO SST anomalies. We developed two simple statistical prediction models for the regional mean SST and its tendency. Regional mean SST and the △SST are the target predictions, which require three predictors: (1) the means of the preceding winter and autumn IOD indexes, (2) the preceding winter's Niño3.4 SST, and (3) the JFM AO index. By fitting to all data samples during

Table 1 Anomalous JJA surface heat fluxes over the western tropical Indian Ocean in association with the JFM AO index during 1984–2009

Regions	Q_{net}	SW	LW	SH	LH
10°N–10°S, 40°–60°E	-5.54^{b}	$+1.54$	-1.86	-0.45^{a}	-4.70^{b}
5°N–5°S, 40°–55°E	-7.92^{b}	$+0.19$	-0.93	-0.63^{a}	-6.73^{b}

Unit: Wm^{-2}

[a] Significant at the 0.1 level, [b] at the 0.05 level

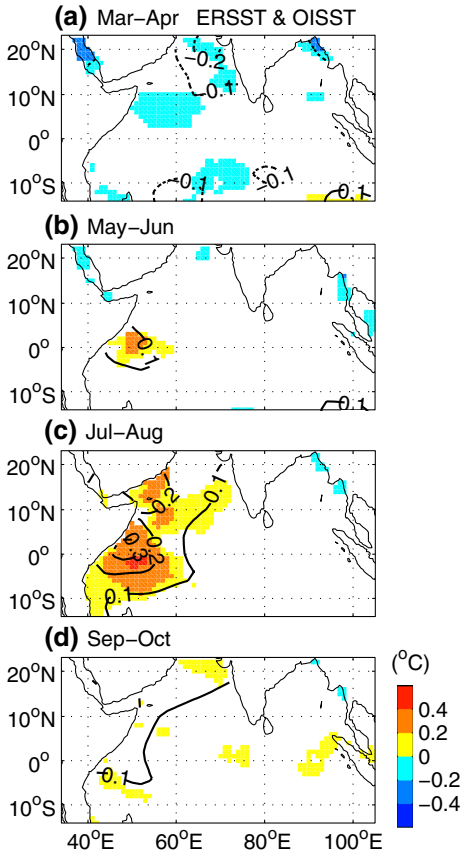

Fig. 1 SST changes from March through October in association with the JFM AO index. The OISST anomalies are shown as *colors* (only values significant at the 0.05 level are plotted) and the ERSST anomalies are overlaid as contour lines with unit of °C. OISST period is 1982–2015, and ERSST data period is 1979–2015

the period 1979–2015, we obtained the corresponding prediction equations as follows:

$$\mathrm{SST} = -0.36\mathrm{IOD} + 0.25\mathrm{Niño3.4} + 0.16\mathrm{AO} \quad (1)$$

$$\triangle\mathrm{SST} = -0.33\mathrm{IOD} + 0.04\mathrm{Niño3.4} + 0.18\mathrm{AO} - 0.01 \quad (2)$$

The SST 'prediction' model yielded a high correlation against the observation ($r = 0.81$), and the △SST model had a similar correlation ($r = 0.79$), suggesting these two models explained $r^2 = 65$ % and $r^2 = 62$ %, respectively, of the observation variance. The linear regression based on all samples tended to encounter the problem of artificial skill produced from over-fitting. The performance of these predictive models was evaluated by cross-validation in a leave-*k*-out strategy (Arlot and Celisse 2010). Here, *k* was the number of samples used as the 'independent' data, a variable that was not used in the training step. To prevent over-fitting or wasting data, the length of the non-overlapping segment of the withheld 'independent' data was suggested to be between 10 and 20 % of the total data length (Hastie et al. 2009; Wilks 2011). In our study, we tested different numbers of *k* varying from 1 to 10. For JJA mean SST, the leave-one-out cross-validation hindcasts and the observations had a correlation of 0.75. Their correlation slightly decreased to 0.72 as the *k* increased to 10. The correlations did not differ much among ten cross-validations, and the mean correlation for ten cases was 0.73. As an example, Fig. 5 displays the hindcasts for cases of $k = 5$ and 10. Both hindcasts agree well with the observations. At the same time, the mean squared error varied from 0.95°C^2 (for $k = 1$) to 1.06 °C^2 (for $k = 10$), with a mean of 1.03 °C^2. The multi-month SST tendency model showed comparable accuracy. The correlations of the predictions and the observations for $k = 1$ and 10 were both 0.70. Again, the results showed little difference among ten *k* cases, with a mean value of 0.68. Meanwhile, the mean squared error increased from 0.99 °C^2 (for $k = 1$) to 1.00 °C^2 (for $k = 10$), with a mean value of 1.03 °C^2. The non-sensitivity of the prediction skills to *k* likely supports the SST's robust and stationary inter-annual linkage to ENSO, the IOD, and (in particular) the AO.

The predictive skills were remarkably smaller when the JFM AO index was excluded from the equations. Based only on the IOD and Niño3.4 indexes, the explained variance for SST and △SST was 31 and 14 %, respectively. Cross-validation for SSTs showed a stable accuracy. For $k = 1$ through 10, the correlations changed little (0.36–0.41) and were notably smaller than the correlations for the AO-included model (by approximately 0.35). At the same time, the mean squared errors were between 1.82 and 1.97 °C^2, results that were evidently larger than the model that included the JFM AO. The △SST model showed a much worse condition. The correlations were quite low and unstable, varying between −0.11 and 0.16 (see Fig. 5d). Therefore, we can conclude that among all three terms in our prediction model, the JFM AO was a major contributing factor for the inter-annual changes of summer SST and, in particular, △SST (see also Fig. 3).

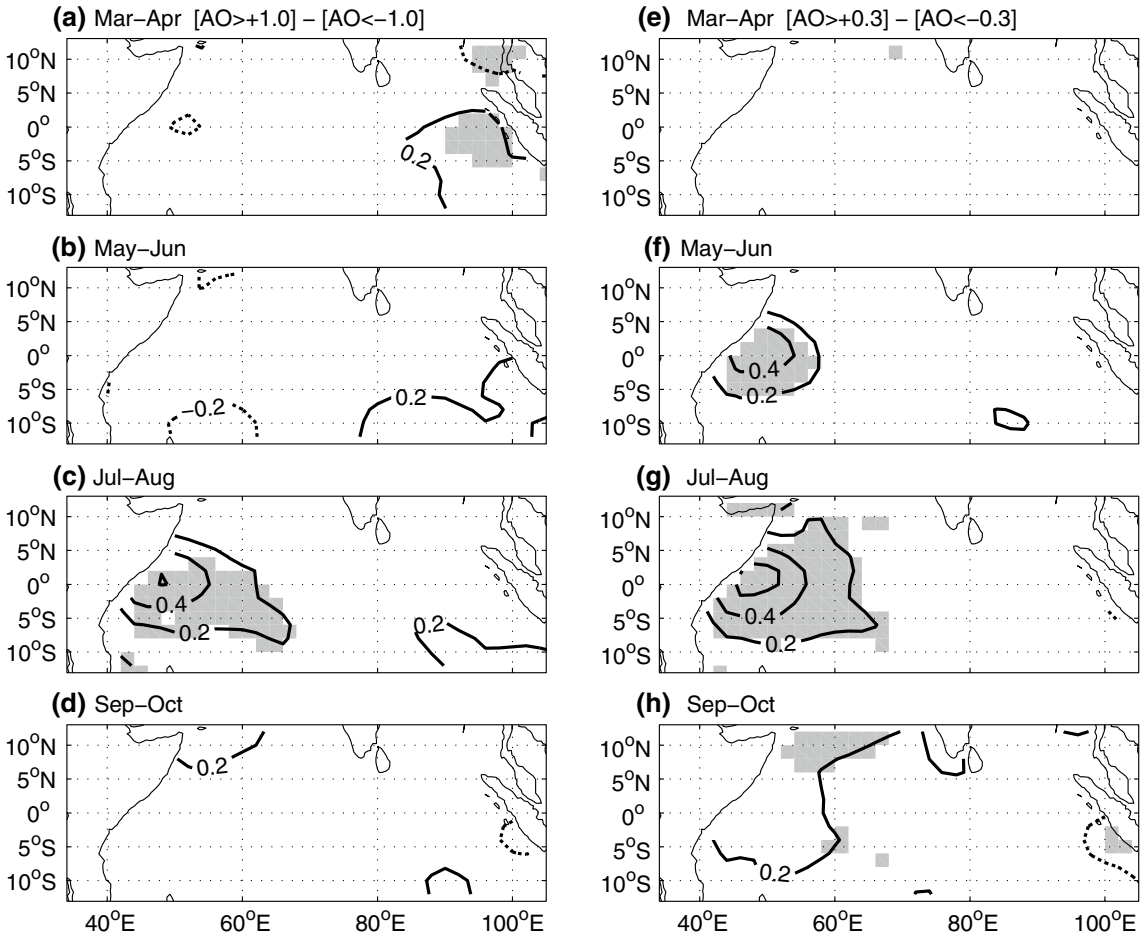

Fig. 2 SST differences of the positive AO years minus the negatives. The positive AO cases are defined as AO $> +1.0$ (or $+0.3$), and the negatives as AO < -1.0 (or -0.3). Positive SST differences are shown as *solid contour lines* and the negatives as the *dashed lines*. The significance levels are estimated from two-sample *t* test and values above the 0.05 level are indicated by *gray shadings*. Results are based on the original, un-filtered ERSST during period 1979–2015

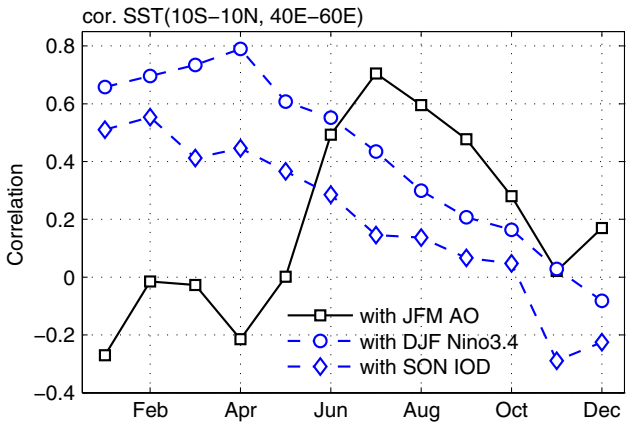

Fig. 3 Correlations between the JFM AO index and monthly ERSST anomalies from January through December over the western tropical Indian Ocean during 1979–2015. The correlations with Niño3.4 SST and IOD are plotted together for comparison

4 Possible mechanisms

4.1 Surface air–sea heat fluxes

One question that arose was what caused anomalous warm SSTs during the summer in association with the winter AO. Over the western TIO, the correlation between SST and the AO index changes from slightly negative in the winter to significantly positive after the spring (Fig. 1), suggesting that the summer warming could not be explained as local/regional SST persistence. On the inter-annual time scale, air–sea heat fluxes and oceanic dynamic processes are two important factors that affect the mixed-layer temperature. First, we examined Q_{net} and its sub-terms (SW, LW, LH and SH). The heat fluxes that warm the upper level of the ocean were defined as of positive sign,

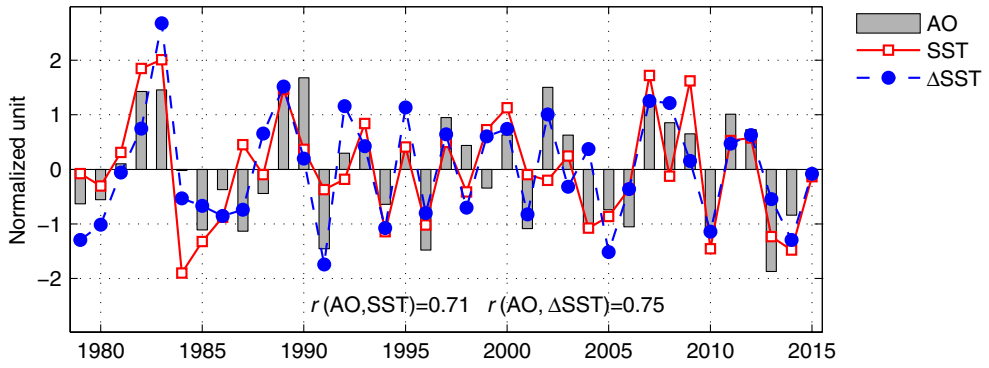

Fig. 4 Timeseries of regional mean JJA SSTs and SST tendency over the western tropical Indian Ocean (10°S–10°N, 40°–60°E). The JFM AO is plotted together for comparison. Multi-month SST tendency (ΔSST) is defined as the SST anomaly difference of June–July–August minus April–May. All are normalized to facilitate comparison

and those that cool the mixed layer were negative; thus, $Q_{net} = SW + LW + LH + SH$. Similar to SST, the least squares fit with the IOD and Niño3.4 SST indexes were estimated and removed from the heat fluxes and then the regression was made. Here, the preceding winter Niño3.4 SST signals and the preceding autumn-winter IOD signals were considered in the regression equations. We found that the net surface heat fluxes were significantly related with the JFM AO variation. As shown in Fig. 6, the negative anomalies appeared in the summer over the western TIO. In association with a one-unit-larger-AO index, the JJA mean Q_{net} decreased by an average of 5.54 Wm^{-2} over the region 10°S–10°N and 40°–60°E. The minimum appeared in July, with a value of -8.70 Wm^{-2}. The JJA mean Q_{net} average over the minimum center (5°S–5°N and 40°–55°E) was $-7.92Wm^{-2}$, and the lowest anomaly also occurred in July, as low as -13.0 Wm^{-2} (Table 1; Fig. 6). Because the Q_{net} comprised four sub-terms, the negative anomalies may have resulted from either more gains or more losses of the heat fluxes. We investigated the SW, LW, SH, and LH and found that the incoming SW changes were not significant. In contrast, the losses of the SH and the LH were significant (Table 1). Particularly, the latent flux for 10°S–10°N and 40°–60°E was $-4.7Wm^{-2}$, and for the center region of 5°S–5°N and 40°–55°E, the LH anomaly was -6.73 Wm^{-2}. According to the bulk formulas for latent and sensible fluxes, three factors (the wind speed, the ocean surface saturation humidity-air humidity difference, and the air–sea temperature difference) must be considered, and these factors are often strongly related. Usually, the wind speed contributes evidently to tropical latent flux (Cayan 1992). In our analysis, the wind speed seemed less important. As shown in Fig. 6, from May through October in the TIO west of 60 °E, there was no anomalous wind velocity change. A comparison of Figs. 1 and 2 may indicate that the enhanced upward sensible and latent fluxes in summer primarily resulted from warmer SST. In sum, the negative Q_{net} implied the ocean lost rather than received heat from the atmosphere. Thus, AO-associated warming SSTs over the western TIO were most likely caused by oceanic dynamics.

4.2 Subsurface temperature changes

We found that the oceanic thermal and dynamic conditions for surface and subsurface layers changed significantly in JJA. After the IOD- and Niño3.4 SST-related variations were fitted and removed, we computed the regression coefficients of JJA sea surface height (SSH) and the depth of the 20 °C isotherm (D20) in association with the JFM AO index (Fig. 7). The depth of the 20 °C isotherm is often used to denote the thermocline over the TIO (e.g., Xie et al. 2002). The salient feature of Fig. 7 is that the above-normal SSH was collocated with a deepened thermocline in the TIO west of approximately 70°E. The SSHs were 1 cm above the normal west of approximately 65°E with a center of >2 cm at approximately 5°–10°S and 50°–60°E. Coincident with SSH anomalies, the thermocline deepened over the western TIO. As can be clearly seen in Fig. 7, the significant JJA D20 anomalies occupied an area between 50°–60°E and 5°–10°S, where the D20 was 4–8 m deeper than normal. The increasing SSH and the deepening of the thermocline in the western TIO implied a suppressed entrainment cooling as well as a weaker upwelling. Both were favorable for warming of the upper ocean.

For more details, we analyzed the vertical temperature profiles using SODA data. As in the composite analysis for SST, we computed the temperature difference of the positive JFM AO cases minus the negatives. For each layer from surface to depth of 400 m, the JJA temperature anomalies over 40°–60°E and 10°S–10°N were averaged. The means for the positive AO years (AO indexes exceeding +0.3) minus those from the negative years (AO indexes below −0.3) were then calculated and plotted in Fig. 8. Above 97 m, positive values were evident. The climatological depth of the thermocline

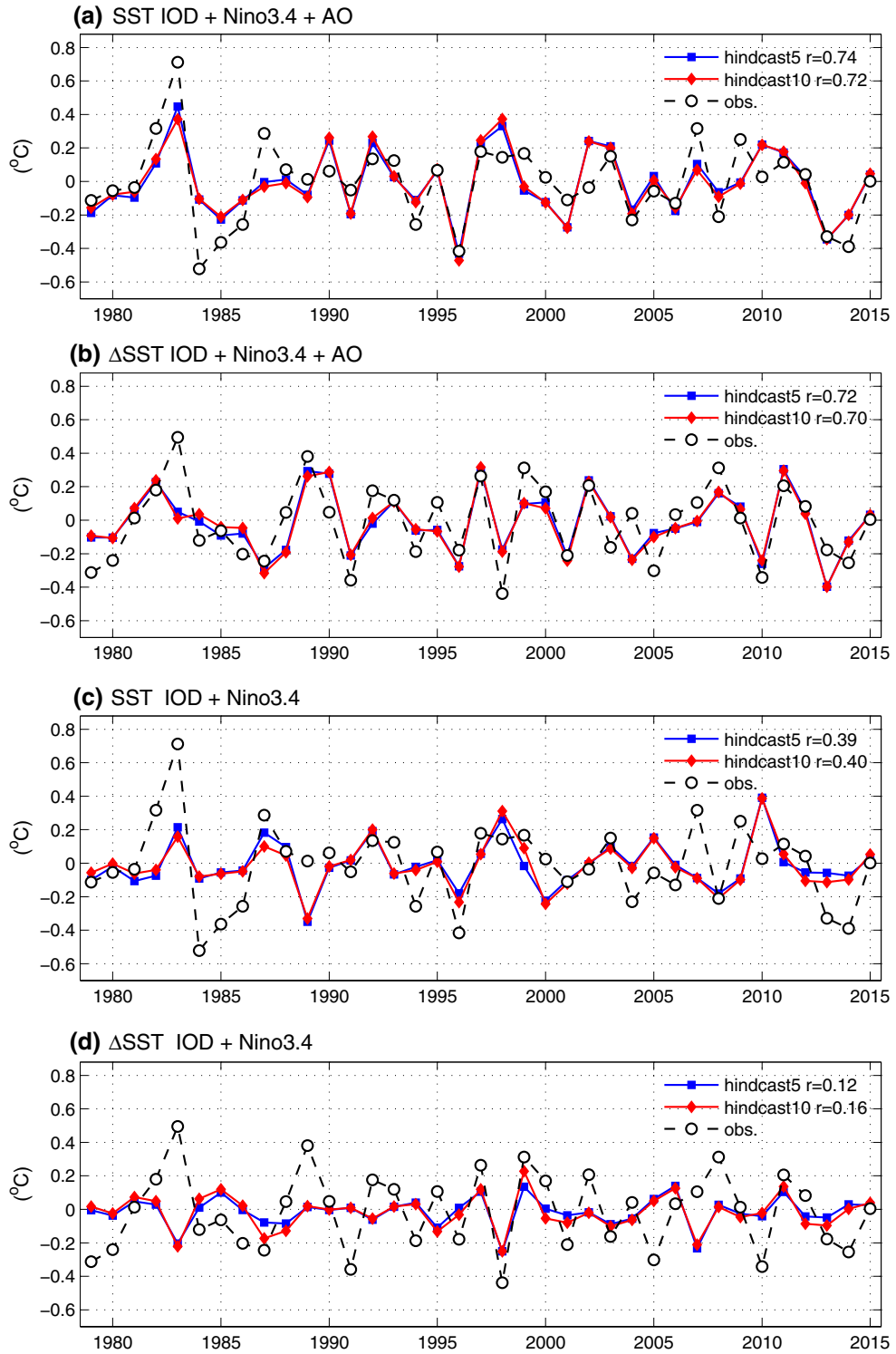

Fig. 5 Interannual SST and ΔSST anomalies in JJA as predicted using the preceding JFM AO index, the preceding winter Niño 3.4 SST and the preceding autumn-winter IOD index (**a**, **b**). Same predictions but without AO are shown in (**c**, **d**). Predictions shown here are made based on a leave-5-out and a leave-10-out cross-validation, labeled as 'hindcast5' and 'hindcast10' respectively

was approximately 90–100 m (Fig. 8a). Therefore, all layers above the thermocline warmed. We also estimated the significance level using Student's *t*-test and found that significant (at the 0.05 level) warming occurred from the surface to 70 m, where temperature anomalies were greater than +0.2 ℃ (Fig. 8b). Meanwhile, the largest temperature

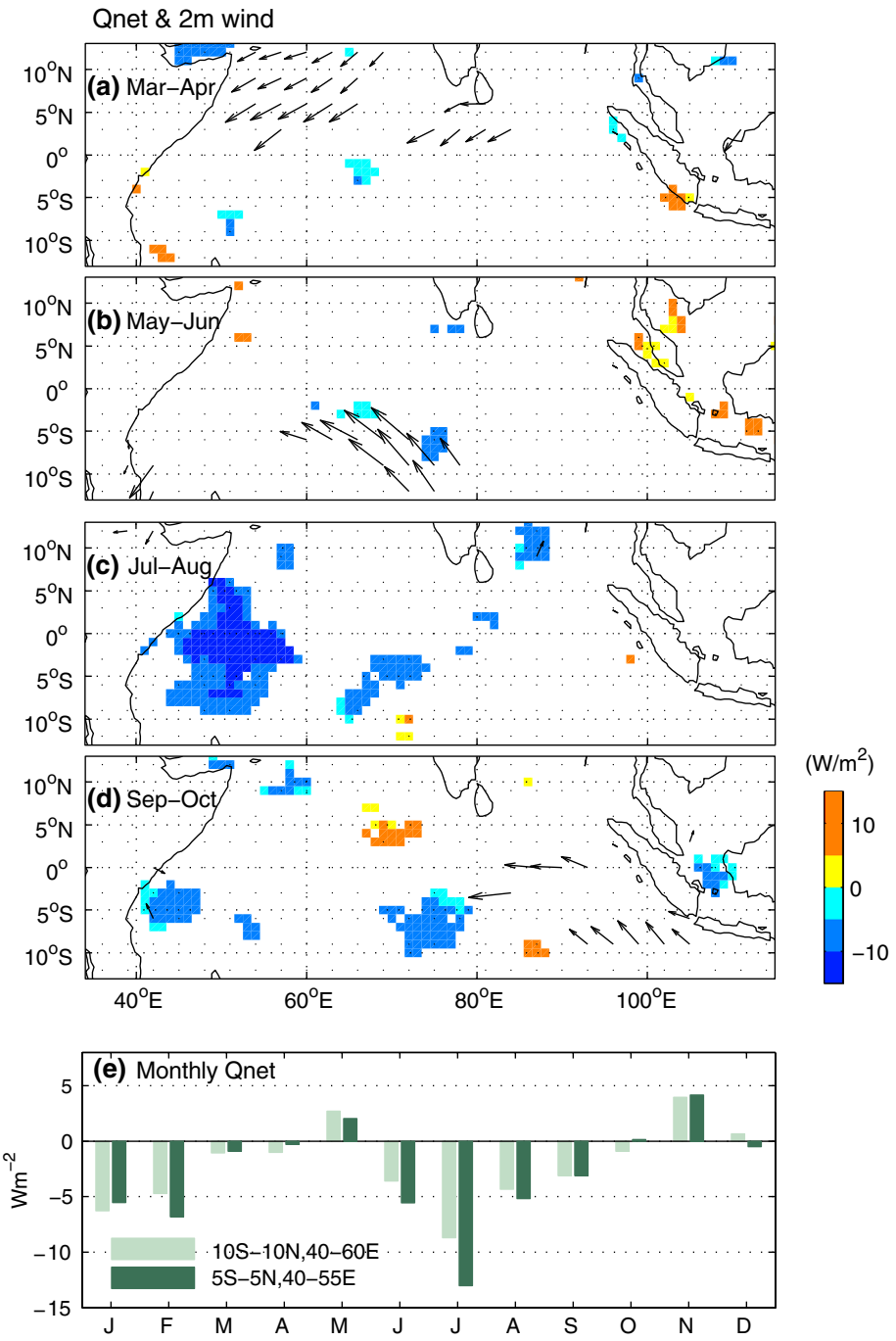

Fig. 6 Net surface heat fluxes (Q_{net}, *colors* in **a**, **b**, **c**, **d**) from March through October in association with the JFM AO index. Vectors in **a**, **b**, **c**, **d** are anomalous 2 m wind velocities from ERA-Interim, and the maximum vector is 0.7 ms^{-1}. Only significant at the 0.05 level Q_{net} and winds are plotted. The regional mean monthly Q_{net} anomalies averaged over the western tropical Indian Ocean are shown in (**e**)

difference appeared between layers 4 and 6 (i.e., at depth of 36–58 m), with a maximum of 0.36°C. Over the tropical Indian Ocean, the mixed-layer depth was between approximately 40 and 50 m during June-July-August (de Boyer Montégut et al. 2004), while its inter-annual variation was two to four times smaller than the seasonal cycle (Keerthi et al. 2013). West of approximately 50°E, the mixed-layer depth evidently increased to 50–60 m.

The question remains as to why anomalous D20 deepened and subsurface warmed in the western TIO during boreal summer in association with the JFM AO variations. Anomalous thermoclines can be directly driven by the local winds or indirectly by oceanic Rossby waves propagating from the east. It is unlikely that the roles of the local winds in summer can explain the oceanic anomalies. The surface scalar wind speed and the cube of the wind speed over the western TIO during JJA showed no evident correlations with the JFM AO (figures not shown), suggesting that the local wind stirring forcing can be ignored. In addition, the JJA wind stress pattern showed no anomalous curl

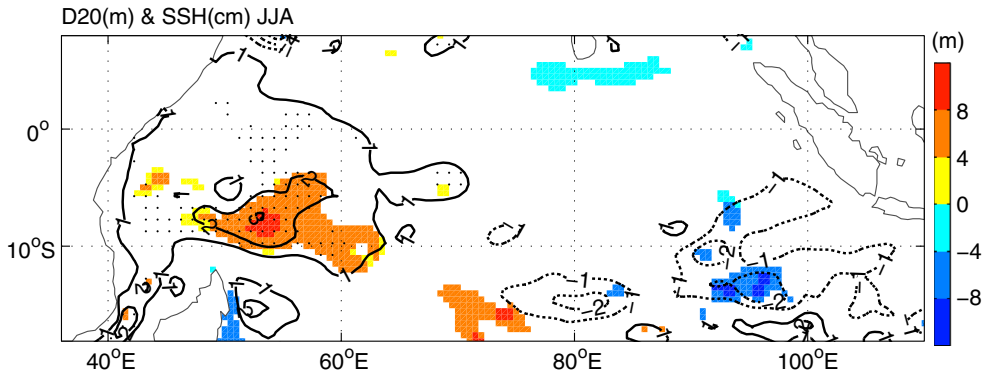

Fig. 7 Anomalies of June–July–August 20°C isotherm depth (D20, *colors*, in meters) and sea surface height (SSH, contour, in centimeters) in association with the JFM AO index. Zero contours are omitted for clarity. Only significant D20 at the 0.05 level are shown. Significant SSHs are indicated by stipples

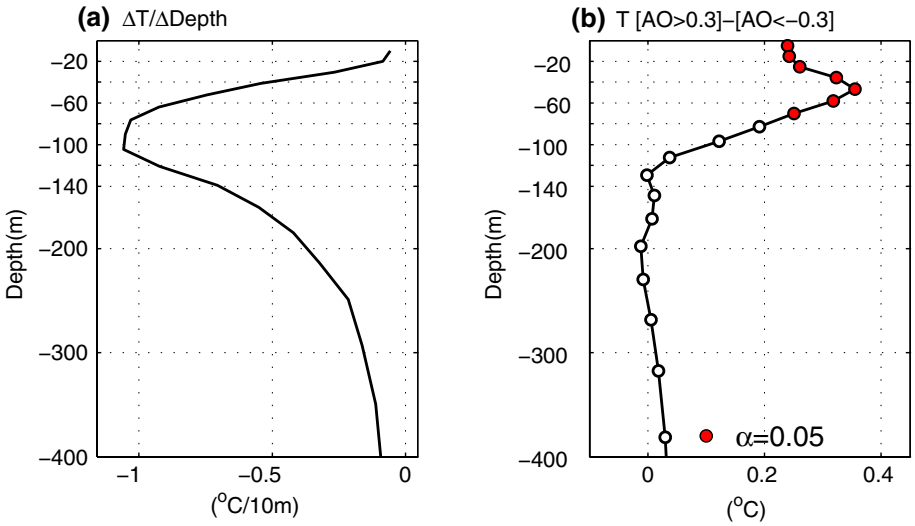

Fig. 8 **a** Long-term mean vertical temperature gradients, **b** the temperature difference of positive AO years (AO> + 0.3) minus the negatives (AO < −0.3). Analysis season is June–July–August, shown are regional means averaging over 40°–60°E and 10°S–10°N. *Filled cycles* indicate the significance level of 0.05

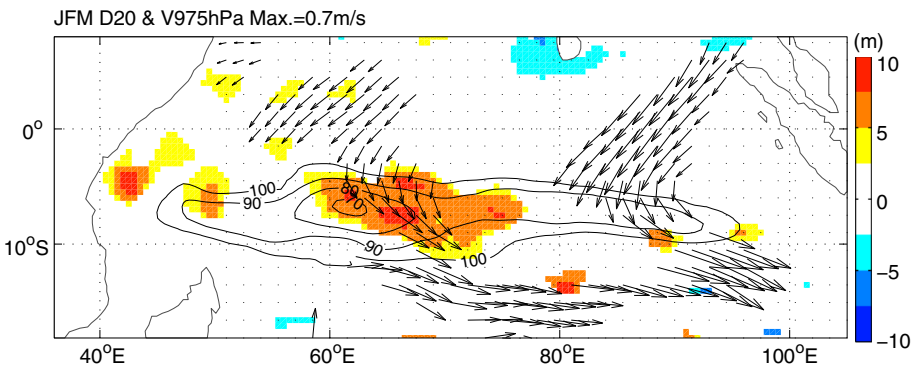

Fig. 9 Anomalies of the 20° C isotherm depth (*contour shadings*, in meters) and ERA-Interim 975 hPa horizontal winds (vectors, in m s^{-1}) corresponding to one unit of AO index during JFM. The long-term mean depth of 20°C isotherm smaller than 100 m are overlaid as contour lines. Only anomalous winds and isotherms significant at the 0.05 level are plotted

(Fig. 6). As demonstrated by numerous studies, oceanic Rossby waves play key roles in low-frequency SST variability in the TIO (e.g., Xie et al. 2002; Huang and Kinter III 2002; Jury and Huang 2004; Schott et al. 2009; among others). These Rossby waves might be generated regionally in the IO, teleconnected to ENSO, or reflected in the eastern boundary by Kelvin waves (Masumoto and Meyers 1998; Xie et al. 2002; Rao and Behera 2005; Nagura and McPhaden 2010; Chakravorty et al. 2013, 2014; Sayantani and Gnanaseelan 2015).

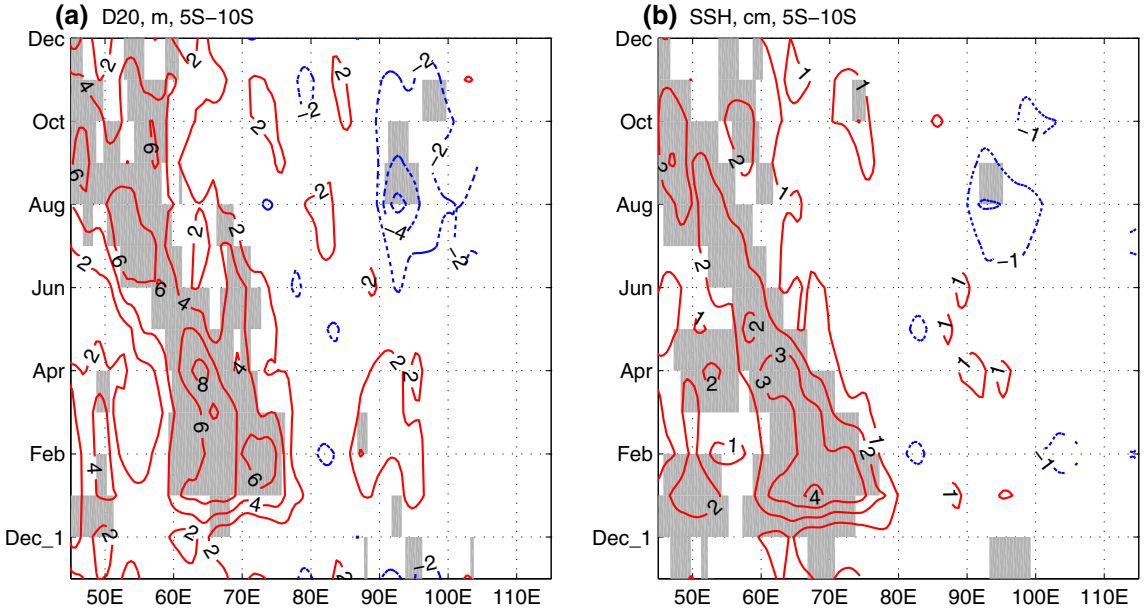

Fig. 10 **a** Anomalous 20 °C isotherm depths and **b** sea surface heights between 5°–10°S in association with one unit of JFM AO index. Significant at the 0.05 level values are indicated by *shadings*

To clarify whether winter AO-related circulation generated oceanic Rossby waves in the Indian Ocean, we examined the simultaneous changes of ERA-Interim 975 hPa winds and D20 in association with the JFM AO indexes. As shown in Fig. 9, two bands of anomalous winds crossed the equator with a C-type pattern: one was located in the central TIO between 60° and 70°E, and another was in the eastern TIO between approximately 80° and 90°E. Correspondingly, the wind stress curl in the central and eastern TIO forced downwelling Ekman pumping. Logically, the D20 deepened significantly over the central TIO, where the anomalies were greater than 5 m, but the change in the eastern TIO was not evident. The reason why anomalous D20 appeared only in the central TIO needs further clarification. The climatological setting of thermocline was likely a possible factor. The climate depth of D20 in the central TIO was smallest over the Indian Ocean; meanwhile, the depth in the east was 10–20 m deeper (see contour lines in Fig. 9). A shallower thermocline implies a greater sensitivity to surface wind stress. A similar pattern of circulation and thermocline changes corresponding to the winter AO was also reported in observation and simulation (e.g., Gong et al. 2014, their figures 4 and 8). Regardless, the co-occurrence of wind anomalies and D20 deepening in the central TIO were robust signals indicative of the AO-related Rossby wave.

In the longitude-time cross sections of the mean D20 and SSH anomalies between 5° and 10°S, we clearly identified their westward propagation (Fig. 10). The anomalous center of D20 moved to 60°E in May and arrived at 50°E in August. An SSH maxima of approximately 2–3 cm was collocated with the moving D20 and traveled simultaneously toward the western TIO. From Fig. 10, we estimated the traveling speed at ~0.14 ms^{-1}, which was approximately the typical oceanic Rossby wave speed (Chelton et al. 1998; Vasala 2008). Note that in the eastern TIO, the D20 was approximately 2 m deeper than normal in JFM, but the anomaly did not travel and vanished after April. In addition, we examined the D20 and SSHs during the preceding winter, as seen in Fig. 10. Before January, no signal was evident, suggesting that the Rossby wave affecting summer in the western TIO was neither generated in the eastern TIO nor radiated from the eastern boundary in the preceding seasons. Rather, it formed in the central TIO during JFM.

As the Rossby wave traveled, the subsurface temperature changed significantly (Fig. 11). During March–April, the temperature was significantly warmer, >0.3°C below 40 m between 60° and 70°E with a maximum of 0.6°C at 60–100 m. In May-June, the center was located at 60°E. In July-August, the location moved to 50°–55°E and the maximum temperature anomaly was as large as >0.6°C at 60–80 m depth. Interestingly, moderate subsurface warming (approximately 0.3°C) occurred above the thermocline at approximately 90°E in March–April, but it disappeared rapidly in May-June. In sum, the salient feature of the subsurface temperature changes was that the largest anomaly traveled from the central TIO in winter to the western TIO in summer along the thermocline. Western TIO SST anomalies resulting from the AO-related Rossby wave were

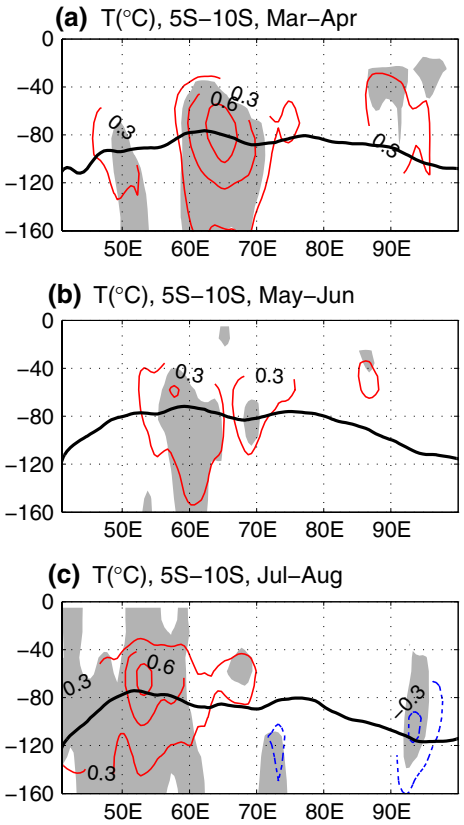

Fig. 11 Anomalies of sea water temperature between 5°–10°S in association with one unit of JFM AO index for each two-month segments from March through August. Significant at the 0.05 level values are *shaded*. *Solid lines* indicate the long-term mean depth of the 20 °C isotherm

consistent with the theoretical baroclinic Rossby wave model and oceanic general circulation model simulations (e.g., Webster et al. 1999; Vasala 2008; Zhuang et al. 2013; Tozuka et al. 2014; Manola et al. 2015).

The AO-related summer warming intensification was different than in winter. In JFM, SST anomalies in the central TIO were not significant, although the thermocline deepened there. In fact, the JFM SST tendency showed significant cooling that was mainly due to the anomalous surface latent heat flux and the decreasing incident short wave radiation (Gong et al. 2014, figures 10 and 11). In summer, AO-related atmospheric forcing no longer existed, whereas the oceanic dynamics dominated the SST variation. For example, Chowdary et al. (2009) showed that the upward propagation of warming associated with the TIO Rossby waves formed a thicker barrier layer. This layer was favorable for anomalous warming above the thermocline and intensified the air–sea coupling over the southwestern Indian Ocean. Such phenomena were not seen in El Niño-induced TIO warming. We assumed that the seasonal atmosphere/ocean configuring might be important. For example, the zonal SST gradient and the mixed layer shoaling (Tozuka et al. 2014) and/or the migration of the ITCZ (Xie et al. 2002) were suggested to play roles in western TIO SST anomalies. The involved local air–sea coupling and feedbacks (Xie et al. 2002; Webber et al. 2010, 2012) might also play roles. The freely propagating Rossby waves behaved very differently from those waves that were damped by air–sea interaction (Xie et al. 2002). This question needs further study for clarification.

5 Numerical experiments

5.1 Model and experiment design

To examine whether the observed AO-SST relationship could be reproduced through oceanic dynamics, we performed numerical experiments using the oceanic component of the Bergen Climate Model, version 2 (BCM2; Furevik et al. 2003; Otterå et al. 2009), which is the Miami Isopycnic Coordinate Ocean Model (MICOM) (Bleck et al. 1992). The horizontal resolution was 2.4° along the equator. The meridional spacing near the equator was 0.8° to better resolve equatorial confined dynamics. The MICOM has 34 isopycnic vertical layers and a non-isopycnic surface mixed layer on top. Previous studies showed that the BCM2 exhibited good performance in simulating the AO as well as the high-latitude Asian climate links (e.g., Luo et al. 2011; Gong et al. 2011, 2014). The MICOM was continuously integrated with the forcing of NCEP-NCAR reanalysis atmospheric circulation from 1948 to 2009. To obtain a stable ocean, the spin-up integration was performed four times with the same atmospheric forcing. Only the last 60 years (1948–2009) were retained to provide the initial condition for the control experiments.

To simulate the possible temperature changes in the Indian Ocean during summer, we performed two parallel atmosphere-forced experiments. The control runs were conducted for 1982 and 1991. These 2 years were chosen as neutral years for the AO, IOD and ENSO (i.e., the JFM AO, the autumn IOD, the preceding autumn IOD, and preceding Niño3.4 SSTs were all within $\pm 0.5\sigma$). The spin-up ocean on January 1, 1982, was selected as the initial condition. Then, it was forced by the NCEP-NCAR reanalysis atmosphere from January 1 through December 31. The integration was repeated 50 times with no interruption. Theoretically, the average of the integrations mimicked the real climate. There were 50 sensitivity runs exactly corresponding to the control runs. For the 1st run, the initial ocean on January 1, 1982 (the same as in the control run), was used. However, AO-related wind stresses over the Indian Ocean were superimposed on the NCEP-NCAR atmosphere from January to March. The ocean integration

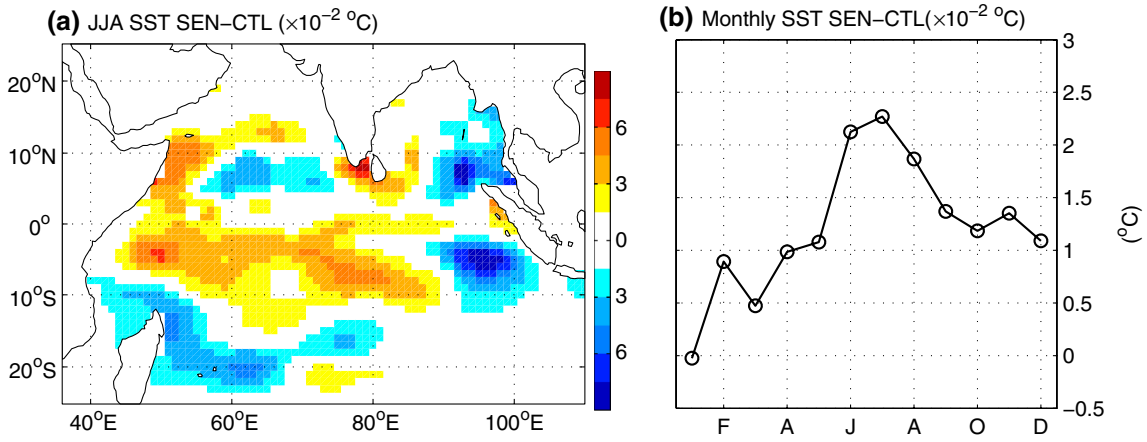

Fig. 12 **a** SST anomalies as the difference of sensitivity runs minus the control runs during JJA, and **b** the regional mean differences averaged over the western Indian Ocean (40°–60°E and 10°S–10°N) from January through December

stopped on December 31. For the other 49 runs, all the initial conditions were taken from the corresponding control runs and the atmospheric forcing was the same as in the first sensitivity run. Therefore, each pair of the 50 sensitivity and control runs started from the same initial conditions. The simulations for year 1991 were run in the same way. To enhance meaningful AO-related signals and to suppress noise, we multiplied the regional mean wind stress climate (0.04 Nm^{-2}) by the significant wind vectors shown in Fig. 9 to build the anomalous forcing flux field. To reduce the possible influence of initial conditions in the ocean, only the last 10 years were retained for both the control and the sensitivity integrations. In total, 20 ensembles were used in our analysis. Then, we computed the means of the 20 ensembles as well as their difference. Ideally, the difference of the sensitivity minus the control runs should be caused by JFM AO-related wind stresses.

5.2 Difference between the sensitivity and control runs

The SST differences between the sensitivity and control runs are shown in Fig. 12. The largest positive SST anomalies were found in the western TIO between 10°S and 10° N and west of 60°E. This was similar to those of the observation regarding location and geographical extent (Fig. 1). Different from observations, negative anomalies appeared close to the east coast, and a moderate positive was located at approximately 80°E between 5°S and 10°S. The monthly mean SST difference over the western TIO (in the same region as the observation) gradually increased from spring to summer and then decreased in autumn and winter. The warming peaked in boreal summer, with a maximum in July. This feature of seasonal evolution was consistent with the observation. SST anomalies in AO-forced simulations were evidently smaller than the observation.

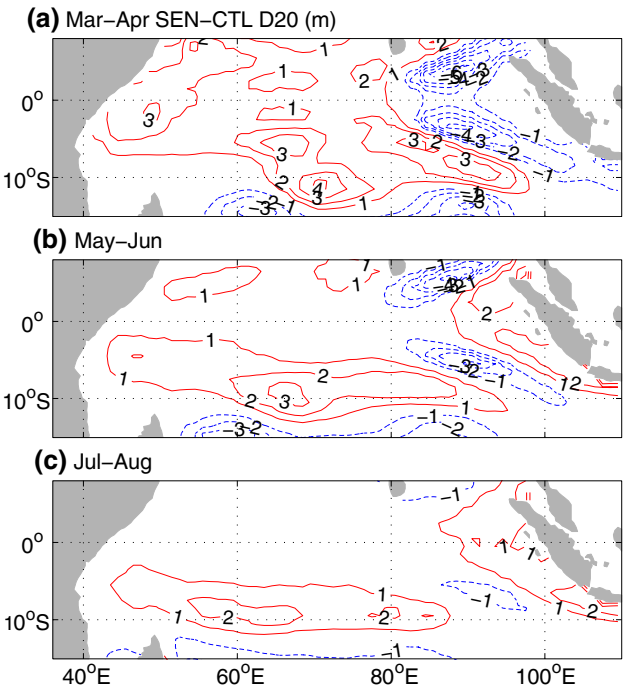

Fig. 13 Simulated 20 °C isotherm depth difference of the sensitivity runs minus the control runs by BCM2.0. Shown as the two-month segments from March through August. Zero contours are omitted for clarity

We further examined the subsurface changes. The D20 difference is shown in Fig. 13. During March–April, two significant positive centers occurred in the southern TIO. One was centered at approximately 90°E and another at approximately 70°E. In both centers, the D20 deepened by 3–4 m. In May-June, the central D20 anomaly moved to 65° E, and in July-August, it traveled to west of 60°E. The D20 anomaly in the eastern TIO did not obviously propagate.

This feature was observed in the longitude-depth cross sections more clearly. Corresponding to the two D20 centers, two collocated positive temperature centers occurred along the thermocline. During March–April, between 85°E and 90°E, the difference was >0.4°C at depths of 70–100 m, and a maximum of >0.6°C occurred at depths of 70–80 m. During the subsequent months, the signals could not be continuously pursued to the west longitudes. As opposed to the eastern TIO, the warming center in the central TIO manifested signs of propagating. In March–April, the largest temperature difference of >0.4 °C was located between 65°E and 70°E; during May–June and July–August, the location moved to approximately 65°E and 55°E, respectively. In short, when forced by the JFM AO-related wind anomalies over the Indian Ocean, our numerical experiments reproduced the Rossby wave activity well. The wave activity was simultaneously generated in the central TIO and then traveled toward the western coast. In addition, the JJA SST warmed because of the arrival of the Rossby waves in the western TIO. In a recent study, Manola et al. (2015) performed numerical experiments using a fully coupled climate model. Forced by the anomalous November and December wind stresses corresponding to the shallow thermocline events over the Seychelles Dome, the model produced westward upwelling Rossby waves and the consequent SST cooling during the subsequent spring and early summer, findings that are consistent with our study.

The simulated oceanic response to AO forcing differed when compared to the observations. In particular, the temperature response was evidently smaller, whereas the response in the eastern Indian Ocean around 85°–90°E was much stronger. This discrepancy likely arises from two factors: (1) the model bias of thermocline and (2) the lack of feedbacks to the atmosphere in the experiments. First, compared with the observation, the thermocline in BCM2 was evidently deeper by approximately 20 m. A deeper thermocline implies a smaller sensitivity to surface wind stress and a smaller mixed-layer temperature change. Similar conditions were also found in other climate models in which a deeper thermocline bias weakened the influence of subsurface variability on SST (e.g., Li et al. 2015). In addition, the model thermocline showed two shallow centers in winter: one located in the western TIO and another in the eastern TIO (compare Figs. 11, 14). The large subsurface temperature change in the eastern TIO was likely due to the shallow bias of the thermocline. We also compared the model mixed-layer depth with the observation (de Boyer Montégut et al. 2004) and found that the model mixed layer depth at 0°–10°S was only 1 m deeper than the observation during JFM but approximately 12 m deeper than the observation in JJA. In particular, the difference

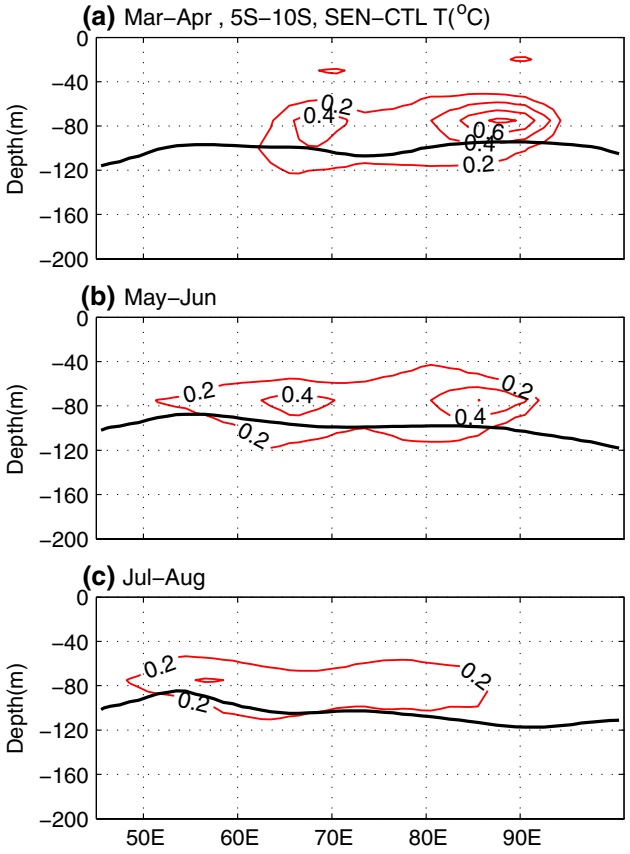

Fig. 14 Difference of sea water temperature between 5°–10°S as the sensitivity runs minus the control runs for each two-month segments from March through August. *Solid lines* indicate the model climate mean depth of the 20°C isotherms

increased to approximately 19 m west of 60°E. A deeper mixed-layer depth bias in summer would be partly responsible for the weaker SST response. Second, our numerical experiments were one-way forced without ocean–atmosphere interaction. As the observations showed, significant anomalies of latent heat occurred in JJA, indicating an enhanced evaporation and increased water vapor. We calculated the JJA specific humidity changes at 2 m in association with the JFM AO index. Not surprisingly, the significant positive anomalies appeared in a large area west of 80°E between 5°S and 10°N with values of >0.1 g kg^{-1}. The maximum of >0.2 g kg^{-1} was located around 50°E (figure not shown). The increased vapor enhanced the long-wave radiations, which, in turn, warmed the ocean (Du and Xie 2008). Wu and Hu (2015) indicated that the changed surface heat fluxes might affect local SSTs, particularly after May over the Arabian Sea. However, these feedbacks were not included in our simulations because after March, the ocean is forced by the normal 'dry' atmosphere.

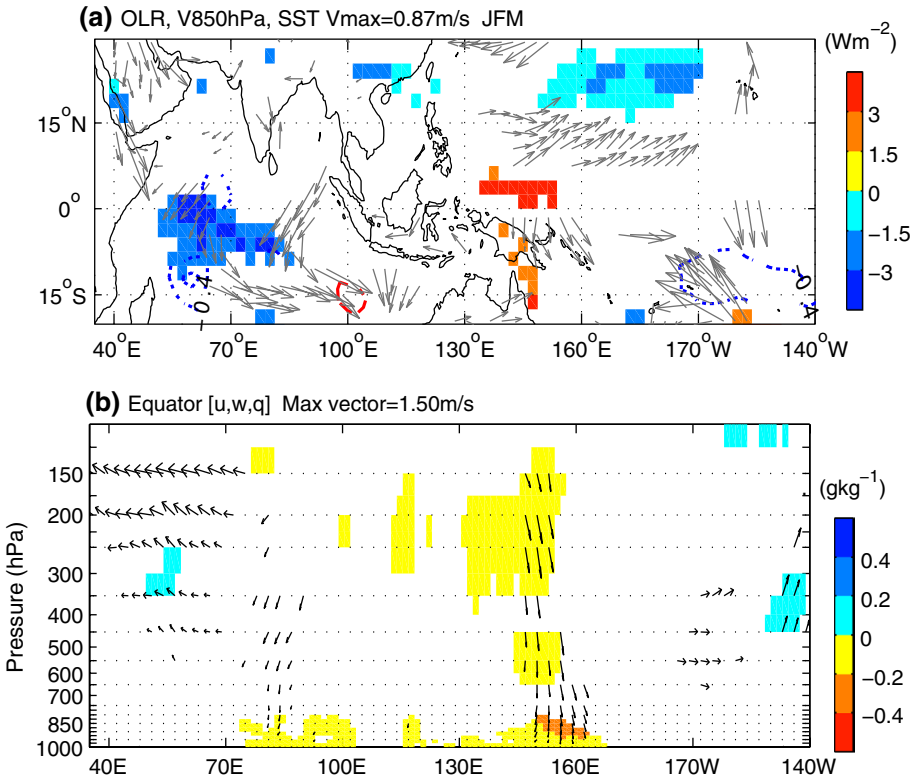

Fig. 15 **a** Anomalies of OLR (*color shadings*, W m^{-2}), horizontal winds at 850 hPa level (vectors, m s^{-1}), and SST (contours, °C) during JFM in association with a unit AO index. **b** Longitude-pressure section along the equator showing anomalous zonal and vertical air motion (vectors, m s^{-1}), and specific humidity (*color shadings*, g kg^{-1}). Only values significant at the 0.05 level are plotted

6 Conclusion and discussion

In the present study, we analyzed the inter-annual linkage between the boreal winter AO and summer SST of the western TIO. It was found that during positive AO years, a significant SST warming occurred in the western TIO. The JJA time series of regional mean SST over the western TIO exhibited an in-phase covariation with the JFM AO index. Their correlation was as large as 0.71 during the period 1979–2015. The AO index also had a high correlation of 0.75 with the SST tendency of changing from a cool April-May to warm JJA. The JFM AO could serve as an effective predictor of JJA SST and its multi-month tendency. Using the JFM AO, the autumn-winter IOD and the winter ENSO, we proposed two statistical prediction models. The variance fitted by the models was 65 and 62 % for SST and the SST tendency, respectively, and their statistical relationship was stable throughout the data period as the cross-validation experiments demonstrated. The analysis of AO-related surface heat fluxes showed that the net heat flux could not explain the western TIO warming because the significant negative net fluxes indicated the ocean loses heat to the atmosphere, whereas the ocean dynamics played a dominant role. During positive AO winters, wind stress curl occurred, causing a downwelling Ekman pumping that forced a deeper thermocline and an above-normal SSH in the central TIO between 60°E and 75°E, where the climatological depth of the thermocline is shallowest in the Indian Ocean tropics. The forced downwelling Rossby wave propagated westward at a speed of approximately 0.14 ms^{-1}. Its arrival in the western TIO resulted in significant warming of the uppermost water. Forced by observed AO wind stress anomalies over the Indian Ocean, the BCM model reasonably reproduced the Rossby wave and the consequent JJA SST warming over the western TIO, supporting the importance of the oceanic dynamics in connecting the winter AO and anomalous summer SSTs.

Previous studies reported that the AO affected tropical western Pacific SST, precipitation, and atmospheric circulation (e.g., Nakamura et al. 2006; Wu 2010; Gong et al. 2011; Chen et al. 2014). Through the AO-triggered anomalous air–sea interaction over the western Pacific, the Indian Ocean's climate might be influenced indirectly. With respect to the equatorial Pacific diabatic heating, there were two possible atmospheric 'bridges.' One was through the Walker Circulation, and another was through the atmospheric Gill-type response. To shed light on this question, we analyzed the JFM AO-related atmospheric circulation, SST and precipitation over the TIO and the western Pacific. As shown in Fig. 15, cyclonic anomalies occurred at the 850 hPa level between 130°E and 170°W north of approximately 10°N. Correspondingly, negative outgoing longwave radiation (OLR) anomalies were located in the center of the cyclonic circulation, indicating increased precipitation. Meanwhile, in the lower latitudes around the equator between 130°E and 160°E, the OLRs tended to

be positive, implying a less active convection. No coherent circulation occurred to the west of the positive OLR anomaly. Furthermore, along the equator over the western Pacific, SST showed no meaningful change, although a cooling appeared between 170°W and 140°W and between 10°S and 15°S. As opposed to SST, the SST tendency exhibited a weak, but significant, positive anomaly of approximately 0.05°C/month along the equator between 160°E and 180°E. In the longitude-pressure section along the equator, descending motions occurred in the central Indian Ocean and easterlies occurred west of 70°E above 500 hPa. These atmospheric motions were caused by the strong anticyclone that was centered over the Arabian Sea (see Gong et al. 2014, their figure 4). In the western Pacific, anomalous descending and drier humidity was located at 150°–160°E. Generally, the JFM equatorial circulation anomalies did not support a potential effect from AO-related anomalies over the Pacific through these two 'bridges.' The AO-Pacific SST linkage was seasonally dependent (Gong et al. 2011; Chen et al. 2015a, b). As opposed to winter, during spring, the AO-related air–sea interaction was much stronger and could persistently influence the East Asian summer monsoon and ENSO (Gong et al. 2011; Chen et al. 2014). The possible roles of the spring AO in modulating Indian Ocean climate require further analysis.

Acknowledgments This study was supported by projects of NSFC-41375071, NSFC-41321001, and 2012GB955401. SJ Kim was supported by project PE16010 of the Korea Polar Research Institute. The SODA datasets were obtained from http://soda.tamu.edu. The air–sea flux data were provided by the WHOI OAFlux project (http://oaflux.whoi.edu) which was funded by the NOAA Climate Observations and Monitoring program. The ERSST and OISST data were provided by the NOAA/OAR/ESRL PSD from their Web site at http://www.esrl.noaa.gov/psd/. The comments and suggestions from two anonymous reviewers were helpful in improving the manuscript.

References

Annamalai H, Liu P, Xie S-P (2005) Southwest Indian Ocean SST variability: its local effects and remote influence on Asian monsoons. J Clim 18:4150–4167

Arlot S, Celisse A (2010) A survey of cross-validation procedures for model selection. Stat Surv 4:40–79

Bleck R, Rooth C, Hu D, Smith LT (1992) Salinity-driven thermocline transients in a wind-and thermohaline-forced isopycnic coordinate model of the North Atlantic. J Phys Oceanogr 22:1486–1505

Carton JA, Giese BS (2008) A reanalysis of ocean climate using Simple Ocean Data Assimilation (SODA). Mon Weather Rev 136:2999–3017

Cayan DR (1992) Latent and sensible heat flux anomalies over the northern oceans: driving the sea surface temperature. J Phys Oceanogr 22:859–881

Chakravorty S, Gnanaseelan C, Chowdary JS, Luo J-J (2014) Relative role of El Niño and IOD forcing on the southern tropical Indian Ocean Rossby waves. J Geophys Res Oceans 119:5105–5122. doi:10.1002/C009713

Chakravorty S, Chowdary JS, Gnanaseelan C (2013) Spring asymmetric mode in the tropical Indian Ocean: role of El Niño and IOD. Clim Dyn 40(5–6):1467–1481. doi:10.1007/s00382-012-1340-1

Chakravorty S, Gnanaseelan C, Pillai PA (2016) Combined influence of remote and local SST forcing on Indian Summer Monsoon Rainfall variability. Clim Dyn. doi:10.1007/s00382-016-2999-5

Chelton DB, deSzoeke RA, Schlax MG, El Naggar K, Siwertz N (1998) Geographical variability of the first baroclinic Rossby radius of deformation. J Phys Oceanogr 28:433–460

Chen S, Yu B, Chen W (2014) An analysis on the physical process of the influence of AO on ENSO. Clim Dyn 42:973–989

Chen S, Yu B, Chen W (2015a) An interdecadal change in the influence of the spring Arctic Oscillation on the subsequent ENSO around the early 1970s. Clim Dyn 44:1109–1126

Chen S, Wu R, Chen W, Yu B (2015b) Influence of the November Arctic Oscillation on the subsequent tropical Pacific sea surface temperature. Int J Climatol. doi:10.1002/joc.4228

Chowdary JS, Gnanaseelan C, Xie SP (2009) Westward propagation of barrier layer formation in the 2006–07 Rossby wave event over the tropical southwest Indian Ocean. Geophys Res Lett 36:L04607. doi:10.1029/2008GL036642

de Boyer Montégut C, Madec G, Fischer AS, Lazar A, Iudicone D (2004) Mixed layer depth over the global ocean: an examination of profile data and a profile-based climatology. J Geophys Res 109:C12003. doi:10.1029/2004JC002378

Du Y, Xie S-P, Huang G, Hu K (2009) Role of air–sea interaction in the long persistence of El Niño-induced North Indian Ocean warming. J Clim 22:2023–2038

Du Y, Xie SP (2008) Role of atmospheric adjustments in the tropical Indian Ocean warming during the 20th century in climate models. Geophys Res Lett. doi:10.1029/2008GL033631

Furevik T, Bentsen M, Drange H, Kindem I, Kvamstø NG, Sorteberg A (2003) Description and validation of the Bergen Climate Model: ARPEGE coupled with MICOM. Clim Dyn 21:27–51

Gnanaseelan C, Vaid BH (2010) Interannual variability in the biannual Rossby waves in the tropical Indian Ocean and its relation to Indian Ocean dipole and El Niño forcing. Ocean Dyn 60(1):27–40

Gong D-Y, Gao Y, Guo D, Mao R, Yang J, Hu M, Gao M (2014) Interannual linkage between Arctic/North Atlantic Oscillation and tropical Indian Ocean precipitation during boreal winter. Clim Dyn 42:1007–1027. doi:10.1007/s00382-013-1681-4

Gong D-Y, Yang J, Kim S-J, Gao Y, Guo D, Zhou T, Hu M (2011) Spring Arctic Oscillation-East Asian summer monsoon connection through circulation changes over the western North Pacific. Clim Dyn 37:2199–2216. doi:10.1007/s00382-011-1041-1

Hastie T, Tibshirani R, Friedman J (2009) The elements of statistical learning: data mining, inference, and prediction, 2nd edn. Springer, Berlin

Huang B, Kinter JL III (2002) The interannual variability in the tropical Indian Ocean. J Geophys Res 107(C11):3199. doi:10.1029/2001JC001278

Izumo T, Montégut CB, Luo J-J, Behera SK, Masson S, Yamagata T (2008) The role of the western Arabian Sea upwelling in Indian monsoon rainfall variability. J Clim 21:5603–5623

Jiang X, Yang S, Li J, Li Y, Hu H, Lian Y (2013) Variability of the Indian Ocean SST and its possible impact on summer western North Pacific anticyclone in the NCEP Climate Forecast System. Clim Dyn 41(7–8):2199–2212

Jury MR, Huang B (2004) The Rossby wave as a key mechanism of Indian Ocean climate variability. Deep-Sea Res I 51:2123–2136

Keerthi MG, Lengaigne M, Vialard J, de Boyer Montégut C, Muraleedharan PM (2013) Interannual variability of the Tropical Indian Ocean mixed layer depth. Clim Dyn 40:743–759

Kug J-S, Jin F-F, An S-I (2009) Two types of El Niño events: Cold tongue El Niño and warm pool El Niño. J Clim 22:1499–1515. doi:10.1175/2008JCLI2624.1

Kumar BP, Vialard J, Lengaigne M, Murty VSN, Foltz GR, McPhaden MJ, Pous S, de Boyer Montégut C (2014) Processes of interannual mixed layer temperature variability in the thermocline ridge of the Indian Ocean. Clim Dyn 43(9):2377–2397. doi:10.1007/s00382-014-2059-y

Lin H, Brunet G, Derome J (2009) An observed connection between the North Atlantic Oscillation and the Madden–Julian Oscillation. J Clim 22:364–380

Lin H, Brunet G (2011) Impact of the North Atlantic Oscillation on the forecast skill of the Madden–Julian Oscillation. Geophys Res Lett 38:L02802. doi:10.1029/2010GL046131

Li G, Xie S-P, Du Y (2015) Climate model errors over the South Indian Ocean thermocline dome and their effect on the basin mode of interannual variability. J Clim 28:3093–3098

Li T, Zhang Y, Lu E, Wang D (2002) Relative role of dynamic and thermodynamic processes in the development of the Indian Ocean dipole: an OGCM diagnosis. Geophys Res Lett 29:2110. doi:10.1029/2002GL015789

Li Y, Wang B, Chang C-P, Zhang Y (2003) A theory for the Indian Ocean dipole-zonal mode. J Atmos Sci 60:2119–2135

Luo FS, Li S, Furevik T (2011) The connection between the Atlantic Multidecadal Oscillation and the Indian summer monsoon in Bergen Climate Model Version 2.0. J Geophys Res 116:D19117. doi:10.1029/2011JD015848

Manola I, Selten FM, de Ruijter WPM, Hazeleger W (2015) The ocean–atmosphere response to wind-induced thermocline changes in the tropical South Western Indian Ocean. Clim Dyn 45:989–1007

Masumoto Y, Meyers G (1998) Forced Rossby waves in the southern tropical Indian Ocean. J Geophys Res 103:27589–27602

McPhaden MJ, Nagura M (2014) Indian Ocean Dipole interpreted in terms of Recharge Oscillator theory. Clim Dyn 42:1569–1586. doi:10.1007/s00382-013-1765-1

Nagura M, McPhaden MJ (2010) Wyrtki Jet dynamics: seasonal variability. J Geophys Res 115:C07009. doi:10.1029/2009JC005922

Nakamura T, Tachibana Y, Honda M, Yamane S (2006) Influence of the northern hemisphere annular mode on ENSO by modulating westerly wind bursts. Geophys Res Lett 33:L07709. doi:10.1029/2005GL025432

Meehl GA, Arblaster JM, Loschnigg J (2003) Coupled ocean–atmosphere dynamical processes in the tropical Indian and Pacific Oceans and the TBO. J Clim 16:2138–2158

NRC (National Research Council of the National Academies) (2010) Assessment of intraseasonal to interannual climate prediction and predictability. National Academies Press, Washington, DC

Otterå OH, Bentsen M, Bethke I, Kvamstø NG (2009) Simulated preindustrial climate in Bergen Climate Model (version 2): model description and large-scale circulation features. Geosci Model Dev 2:197–212

Pan LL, Li T (2008) Interactions between the tropical ISO and midlatitude low-frequency flow. Clim Dyn 31:375–388

Rao SA, Dhakate AR, Saha SK, Mahapatra S, Chaudhari HS, Pokhrel S, Sahu SK (2012) Why is Indian Ocean warming consistently? Clim Change 110:709–719. doi:10.1007/s10584-011-0121-x

Rao SA, Behera SK (2005) Subsurface influence on SST in the tropical Indian Ocean: structure and interannual variability. Dyn Atmos Oceans 39:103–135

Reynolds RW, Rayner NA, Smith TM, Stokes DC, Wang W (2002) An improved in situ and satellite SST analysis for climate. J Clim 15:1609–1625

Saji NH, Goswami BN, Vinayachandran PN, Yamagata T (1999) A dipole mode in the tropical Indian Ocean. Nature 401:360–363

Sayantani O, Gnanaseelan C (2015) Tropical Indian Ocean subsurface temperature variability and the forcing mechanisms. Clim Dyn 44:2447–2462

Schott FA, Xie S-P, McCreary P Jr (2009) Indian Ocean circulation and climate variability. Rev Geophys 47:RG1002. doi:10.1029/2007RG000245

Seiki A, Katsumata M, Horii T, Hasegawa T, Richards KJ, Yoneyama K, Shirooka R (2013) Abrupt cooling associated with the oceanic Rossby wave and lateral advection during CINDY2011. J Geophys Res Oceans 118:5523–5535. doi:10.1002/jgrc.20381

Smith TM, Reynolds RW, Peterson TC, Lawrimore J (2008) Improvements to NOAA's historical merged land-ocean surface temperature analysis (1880–2006). J Clim 21:2283–2296

Taschetto AS, Ambrizzi T (2012) Can Indian Ocean SST anomalies influence South American rainfall? Clim Dyn 38:1615–1628

Taschetto AS, Gupta AS, Hendon HH, Ummenhofer CC, England MH (2011) The contribution of Indian Ocean sea surface temperature anomalies on Australian summer rainfall during El Niño events. J Clim 24(14):3734–3747

Trenary LL, Han W (2012) Intraseasonal-to-interannual variability of South Indian Ocean sea level and thermocline: remote versus local forcing. J Phys Oceanogr 42:602–607

Tozuka T, Nagura M, Yamagata T (2014) Influence of the reflected Rossby waves on the western Arabian Sea upwelling region. J Phys Oceanogr 44:1424–1438

Vasala V (2008) First and second baroclinic mode response of the tropical Indian Ocean to interannual equatorial wind anomalies. J Oceanogr 64:479–494

Wang X, Jiang X, Yang S, Li Y (2013) Different impacts of the two types of El Niño on Asian summer monsoon onset. Environ Res Lett 8(4):044053. doi:10.1088/1748-9326/8/4/044053

Webber BGM, Matthews AJ, Heywood KJ (2010) A dynamical ocean feedback mechanism for the Madden–Julian Oscillation. Q J R Meteorol Soc 136:740–754

Webber BGM, Matthews AJ, Heywood KJ, Stevens DP (2012) Ocean Rossby waves as a triggering mechanism for primary Madden–Julian events. Q J R Meteorol Soc 138:514–527

Webster PJ, Moore AM, Loschnigg JP, Leben RR (1999) Coupled ocean–atmosphere dynamics in the Indian Ocean during 1997–98. Nature 401:356–360

Weng H, Ashok K, Behera SK, Rao SA, Yamagata T (2007) Impacts of recent El Niño Modoki on dry/wet conditions in the Pacific rim during boreal summer. Clim Dyn 29:113–129. doi:10.1007/s00382-007-0234-0

Wilks DS (2011) Statistical methods in the atmospheric sciences, 3rd edn. Academic Press, London

Wu Q (2010) Forcing of tropical SST anomalies by wintertime AO-like variability. J Clim 23:2465–2472

Wu R, Kirtman BP, Krishnamurthy V (2008) An asymmetric mode of tropical Indian Ocean rainfall variability in boreal spring. J Geophys Res 113:D05104. doi:10.1029/2009/2007jd009316

Wu R, Yeh S-W (2010) A further study of the tropical Indian Ocean asymmetric mode in boreal spring. J Geophys Res 115:D08101. doi:10.1029/2009jd012999

Wu R, Hu W (2015) Air-sea relationship association with precipitation anomaly changes and mean precipitation anomaly over the South China Sea and the Arabian Sea during the spring to summer transition. J Clim 28:7161–7181

Xiang B, Yu W, Li T, Wang B (2011) The critical role of the boreal summer mean state in the development of the IOD. Geophys Res Lett 38:L02710. doi:10.1029/2010GL045851

Xie S-P, Annamalai H, Schott FA, McCreary JP (2002) Structure and mechanisms of south Indian Ocean climate variability. J Clim 15:867–878

Xie S-P, Hu K, Hafner J, Tokinaga H, Du Y, Huang G, Sampe T (2009) Indian Ocean capacitor effect on Indo-Western Pacific climate during the summer following El Niño. J Clim 22:730–747

Yu W, Xiang B, Liu L, Liu N (2005) Understanding the origins of interannual thermocline variations in the tropical Indian Ocean. Geophys Res Lett 32:L24706. doi:10.1029/2005GL024327

Yu L, Jin X, Weller RA (2008) Multidecade global flux datasets from the Objectively Analyzed Air-Sea Fluxes (OAFlux) project: latent and sensible heat fluxes, ocean evaporation, and related surface meteorological variables. Woods Hole Oceanographic Institution OAFlux Project Tech. Rep. OA-2008-01, 64 pp

Yuan J, Feldstein SB, Lee S, Tan B (2011) The relationship between the North Atlantic jet and tropical convection over the Indian and western Pacific Oceans. J Clim 24:6100–6113

Zhou S, Miller AJ (2005) The interaction of the Madden–Julian Oscillation and the Arctic Oscillation. J Clim 18:143–159

Zhu J, Huang B, Kumar A, Kinter JL III (2015) Seasonality in prediction skill and predictable pattern of tropical Indian Ocean SST. J Clim 28:7962–7984

Zhuang W, Feng M, Du Y, Schiller A, Wang D (2013) Low-frequency sea level variability in the southern Indian Ocean and its impacts on the oceanic meridional transports. J Geophys Res Oceans 118:1302–1315. doi:10.1002/jgrc.20129